INTERNATIONAL JOURNAL FOR NUMERICAL METHODS IN FLUIDS
Int. J. Numer. Meth. Fluids 2002; **39**:465–483 (DOI: 10.1002/fld.246)

A numerical and experimental study of batch sedimentation and viscous resuspension

Rekha Rao[1,*], Lisa Mondy[1], Amy Sun[1] and Steve Altobelli[2]

[1]*Sandia National Laboratories, Albuquerque, NM 87185, U.S.A.*
[2]*New Mexico Resonance, Suite C1, Yale Center, Albuquerque, NM 87108, U.S.A.*

SUMMARY

A suspension of non-neutrally buoyant, large, nearly monodisperse spheres is studied both in batch sedimentation and in shear between concentric rotating cylinders. We apply a continuum constitutive equation based on the diffusive flux model augmented with buoyancy terms derived by Acrivos and coworkers and discretize the resulting equation set with the finite element method. We simulate batch sedimentation using this method and obtain a reasonable match with experiment. Next used two-dimensional NMR imaging to measure the evolution of solid fraction profiles in the same suspension undergoing flow between rotating concentric cylinders with two different initial conditions. Here, both gravity-induced and shear-induced particle migration are significant. Under these conditions, we have found that simulating the correct initial condition is critical to matching the experimental results. When this is done, the model results compare well with the experiments. Copyright © 2002 John Wiley & Sons, Ltd.

KEY WORDS: shear flows; batch sedimentation; viscous resuspension, Couette flow

INTRODUCTION

Particle-laden shear flows are important in a wide variety of applications in oil and gas production and in the mineral, chemical and food processing industries. These include such application as batch sedimentation, hydraulic fracturing technology and slurry transport. Particle separation due to density differences occurs in many non-colloidal mixtures of particles and liquids, and many processing activities can benefit from knowledge of the physics of systems undergoing sedimentation or flotation. For this reason, we are trying to develop a modeling capability that allows us to predict the flow and particle transport properties of arbitrary buoyant suspensions in complex geometries.

It is now well known that flowing suspensions of particles in a liquid have been known to exhibit particle migration even in creeping flow and in the absence of significant nonhydrodynamic or gravitational effects [1–3]. In particular, Leighton and Acrivos [2] proposed scaling arguments that identified three causes of particle migration, namely, gradients in shear rate,

*Correspondence to: R. Rao, Sandia National Laboratories, Albuquerque, NM 87185, U.S.A.

Received 10 May 2001
Revised 14 August 2001

concentration, and relative viscosity. These arguments are the basis of a constitutive model for the evolution of particle concentration in a flowing suspension proposed by Phillips *et al.* [4] and referred to as the diffusive flux model. This constitutive description couples a generalized Newtonian momentum equation where the local viscosity of the suspension is dependent on the local volume fraction of solids with an evolution equation to describe the shear-induced migration of the suspended particles. Subia *et al.* [5] extended the diffusive flux model from viscometric to multidimensional flows using a scalar shear rate invariant to describe the shear-induced migration and solved the resulting equations with the finite element method. They obtained excellent agreement between the modeling results and NMR imaging of the particle concentration.

The term viscous resuspension was first used by Leighton and Acrivos [6] to describe the resuspension of sedimented particles due to shear flow. Complex flow and particles profiles can arise resulting from a balance of gravitational flux on the particles, which tends to lead to segregation, with shear-induced migration, which can cause remixing. A number of experimental studies have been carried out to look at the effects of viscous resuspension in pipe, channel and Couette geometries [7–11]. However, little work has been done on computational modeling of viscous resuspension. Most of the existing modeling work has been at the particle-level, which though elucidating, can be computationally intensive and difficult to apply to arbitrary geometries [12–14]. Continuum approaches have a greater chance of being useful for modeling a variety of flow fields and suspensions. However, much of the continuum modeling work has used simplified equations that are either analytically tractable or solved with rudimentary numerical methods [15]. For instance, Shauly *et al.* [16] modeled viscous resuspension in a polydisperse system and looked at a variety of geometries, but simplified the equations to examine one-dimensional flows only. Miskin *et al.* [17, 18] model viscous resuspension in channel flows, but simplify the equations to two-dimensions and use a specialized finite difference method.

One exception is the pivotal work of Zhang and Acrivos [19] who formulated a general numerical approach to modeling multidimensional viscous resuspension with few simplifying assumptions. They used a continuum approach and extended the work of Leighton and Acrivos [2] to non-neutrally buoyant suspensions with the inclusion of a hindered settling function in the particle evolution equation and a buoyancy term in the momentum equation. They discretized the theoretical model with the finite element method and examined fully developed flow profiles in a pipe flow and obtained good agreement with experiment.

Here we examine the applicability of a continuum model of viscous resuspension and base much of our work on that of Zhang and Acrivos [19] and Phillips *et al.* [4], with some significant modifications. We simulate the behavior of concentrated suspensions of large, monodisperse spheres with a Galerkin, finite element, Navier–Stokes solver into which is incorporated a continuum constitutive relationship based on the diffusive flux model but modified to allow gravity effects. Results of the model are compared with experiment. The experiments involve using nuclear magnetic resonance (NMR) imaging to determine noninvasively the evolution of the solids-concentration profiles of suspensions as they separate when subjected to a variety of slow flows in which gravity has a substantial effect. The model is first tested on batch sedimentation to insure the correct form of the hindered settling function was used. Once the model was validated for settling without flow, a more complex problem was simulated that included shear as well as buoyancy effects. The problem studied was viscous resuspension in a large-gap Couette from two different initial conditions. The first initial

condition was a well-mixed, homogeneous suspension while the second was a fully sedimented suspension.

In the following section we describe the experimental procedure: the batch sedimentation experiments in the first subsection and the wide-gap Couette experiments in the second. The model is described in the next section, including discussion about the equations and numerical method. In the final section we give the problem definition and present the results, both of the model and experiment, and discuss the comparison between them.

EXPERIMENTS

Batch sedimentation

A single particle in a non-neutrally buoyant fluid will fall at a rate given by its Stokes velocity, which is related to the particle and the fluid properties as well as gravity. For a suspension of particles, the behavior is more complex (see for instance Probstein [20] for an excellent discussion of sedimentation). An initially well-mixed non-neutrally buoyant suspension will separate into three different phases as shown in Figure 1. For heavy particles, a sediment will form at the bottom of the container approaching the maximum packing particle concentration, with a well-mixed suspension in the middle of the container at the average concentration and a clear zone of fluid at the top of the container, which is particle free. At the phase boundaries there are discontinuities in densities and velocity that are termed kinematic shocks. The phase boundaries move toward each other at velocities that can be worked out using the one-dimensional theory of Kynch [21]. The motion of the phase boundaries is related to the Stokes velocity and a hindered settling function [22]. For a suspension of particles, the hindered settling function is necessary to account for the fact that the particles are not settling as single spheres, as was assumed when deriving the Stokes velocity, but interact with their neighbor particles as they settle. Once these two shock fronts have come together, the final state of the suspension has only two remaining phases; sediment and pure fluid.

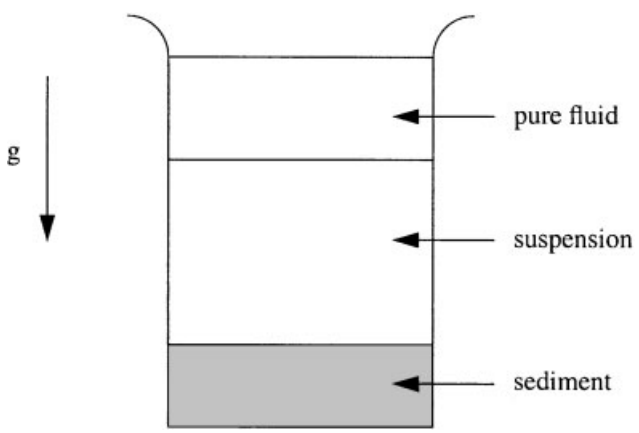

Figure 1. Batch sedimentation from an initially well mixed suspension.

Table I. Density, viscosity, and particle data for PMMA experiments.

Quantity	Value
density PMMA, ρ_s^0	1.18 g cm^{-3}
density glycerol/water solution, ρ_f^0	1.253 g cm^{-3}
viscosity glycerol/water solution, μ_0	5.889 g cm^{-1} s^{-1}
maximum volume fraction, $\phi_{\max}$	0.58, 0.64
initial volume fraction, ϕ_0	0.20
particle radius, a	0.0397 cm

The sign of the density difference between the solid phase and the liquid phase determines whether the particles will sediment or float; aside from the direction of solid motion there is no difference between the two processes for the purposes of this paper. In this work, descriptions are given in terms of flotation, where the dispersed phase is rising and the continuous phase is sinking.

Previous NMR studies have demonstrated that imaging may be used to observe shear-induced particle migration [3], to measure the hindered settling function by observing the clearing layer [23], and also to study interfacial broadening [24]. In this paper, we first use one-dimensional NMR to determine the liquid fraction as a function of the vertical coordinate and time. Two-dimensional NMR imaging of batch sedimentation shows that the assumed one-dimensional nature of the concentration profile is true; however, the velocity is not one-dimensional.

The flotation experiments were performed in acrylic right circular cylinders. The ID of the cylinders was 3.75 ± 0.01 cm and the suspension samples were 4.0 ± 0.1 cm deep, which made the total volume of the samples 44 ± 1 ml. The height of the sample vessel is restricted by the small imaging volume available in our horizontal magnet, and so our results are not directly comparable to many previous studies. The limitation is not inherent in the technique, but rather in the scale of our particular instrument.

The suspending liquid was nominally 96 per cent glycerol, 4 per cent water by weight. The longitudinal relaxation time T_l of the liquid was 0.3 ± 0.1 s. The solid phase was 0.0794 cm diameter polymethyl methacrylate (PMMA) spheres. An isolated particle of the average size would have a Reynolds number $< 10^{-6}$ and a Peclet number $> 10^{10}$, and a Stokes settling velocity of 3.7×10^{-3} cm s^{-1}. Table I lists the relevant properties of the suspension and its components. The maximum volume fraction was taken from the maximum value of the one-dimensional NMR images described below. However, it has been found that this maximum concentration increases over time as consolidation occurs to the theoretical value for maximum packing which is 0.64 for random closed pack spheres. As discussed in the numerical modeling section, the value of 0.64 is also optimal for matching the viscosity data. Thus, 0.58 was used in the early-time batch sedimentation study while 0.64 was used for the Couette studies.

The suspension was well mixed immediately prior to the experiments and then placed in the bore of the magnet. Through visual observation, we noted that flow due to the mixing ceased quickly, well before the initial NMR image was taken.

Proton ^{1}H NMR experiments [25] were performed in a 1.89 T, 31 cm bore, horizontal, superconducting magnet. A one-dimensional NMR technique produced a measurement of the amount of liquid as a function of the height averaged over a 16.32–64.32 s period. The solid phase produces no NMR signal in this experiment. Since the total height of the suspension is

monitored and does not change in the course of the experiment, we assume there is no significant volume of air bubbles so that the solid fraction is directly measured. Two-dimensional imaging, which takes significantly more time per image, was also performed to confirm that the concentration was uniform on average at any one height.

Wide-gap Couette experiments

Nuclear magnetic resonance (NMR) imaging was also used to measure the concentration profile during the demixing of an initially well-mixed suspension of the same non-neutrally buoyant particles and liquid as described above. A suspension was placed between two concentric cylinders (wide-gap Couette), the inner cylinder of which rotated while the outer remained fixed. The Couette device was placed in the horizontal bore magnet with the Couette axis parallel to the bore axis. An inhomogeneous shear flow field is produced in the wide gap of the Couette device. Because of this, the suspended particles will migrate toward the low shear rate region near the outer cylinder walls, even though in these experiments the conditions are such that colloidal and inertial forces do not exert an appreciable effect on the suspensions. However, gravity is also acting on the suspension causing the particles to float toward the upper surface.

The techniques used in these experiments remain essentially the same as those described by Abbott *et al.* [3]. The outer radius of the inner rod (R_i) was 0.64cm and the inner radius of the outer cylinder (R_o) was 2.54cm, and the length of the suspension-filled cavity was 25cm. The shaft was turned at a steady rate of 55 revolutions per minute. NMR images were taken of a cross-sectional slice, 10-mm thick, perpendicular to the Couette axis, about midway along the apparatus. The time required for each image was about four minutes. In these experiments the intensity values in the part of the slice corresponding to the Couette were normalized with a pure fluid blank. As in the batch settling experiments, the solid particles produced no signal, so the intensity of the image yielded directly the volume fraction of liquid (and, hence, particles).

Two types of Couette flow experiments were carried out. In the first study, a suspension of 35 per cent by volume of particles was mixed well and then loaded as rapidly as possible into the Couette apparatus, then the apparatus was loaded into the magnet. However, this process took several minutes, and taking the initial image also took several minutes. During this time the particles were beginning to separate due to buoyancy. The motor was started as soon as the initial image was completed. During subsequent image collection, the motor was not stopped. In the second experiment, a suspension of 20 per cent by volume of particles was allowed to reach equilibrium overnight inside a stationary Couette. The motor did not start and the images were not collected until all the particles had floated to the top.

NUMERICAL MODEL

Equations

A model based on previous work by Phillips *et al.* [4] and Zhang and Acrivos [19] was used to predict the particle concentration evolution. One of the key features of this model is the density difference between the fluid and the particle phases, which introduces a variable

density throughout the flow regime. Let ρ_ϕ and ρ_s be the mass concentrations of the fluid phase and particle phase, respectively. Thus,

$$\rho_f = (1-\phi)\rho_f^0 \tag{1}$$

$$\rho_s = \phi\rho_s^0 \tag{2}$$

where ϕ is the particle-phase volume fraction ρ_f^0 and ρ_s^0 are the pure phase densities. We also define the total mixture density as,

$$\rho = \rho_f + \rho_s = (1-\phi)\rho_f^0 + \phi\rho_s^0 \tag{3}$$

Hence, the suspension density is not constant, but depends on particle concentration. This introduces as Boussinesq-like, buoyancy driven flow term in the momentum equation.

The momentum equation is further complicated by the particle-concentration dependent, non-Newtonian viscosity.

$$\rho\frac{\partial v}{\partial t} + \rho\mathbf{v}\cdot\nabla\mathbf{v} + \nabla p - \nabla\cdot(\mu(\nabla v + \nabla v^t)) - (\rho_f^0 - \rho_s^0)\phi\mathbf{g} = 0 \tag{4}$$

where $\mathbf{v}$ is the suspension velocity, p is the dynamic pressure, $\mathbf{g}$ is the gravitational acceleration, and t is time. Note that the constant portion of the momentum source has been absorbed by the dynamic pressure. This tends to create a more stable numerical implementation for buoyancy driven flows, since the system will be more responsive to changes in the source term.

The viscosity depends on the particle concentration. Its behavior is quite nonlinear, ranging from highly viscous solid-like behavior at the limit of maximum packing (ϕ_m) to much lower viscosity in the pure fluid (μ_0) region. Here we use a Krieger form for the viscosity model [26], since it is found to agree well with experimental data. In this model, n is a parameter that is used to best fit the viscosity data.

$$\mu = \mu_0\left(1 - \frac{\phi}{\phi_m}\right)^{-n} \tag{5}$$

In Figure 2 we show results of Equation (5) compared to literature values collected by Thomas [27]. These values have been shown to agree with falling ball and spinning ball measurements on similar suspensions to those used in this study [28].

Though each phase is incompressible and the continuum is incompressible, the continuity equation will no longer be solenoidal, due to the density difference between particles and carrier fluid. This introduces the particle flux, $\mathbf{J}_s$ into the continuity equation.

$$\nabla\cdot v = \frac{(\rho_s^0 - \rho_f^0)}{\rho_s^0\rho_f^0}\nabla\cdot J_s \tag{6}$$

To determine the particle flux, we write a particle conservation equation in the standard manner.

$$\frac{\partial\phi}{\partial t} + \nabla\cdot(\phi\mathbf{v}) = -\frac{\nabla\cdot J_s}{\rho_s^0} \tag{7}$$

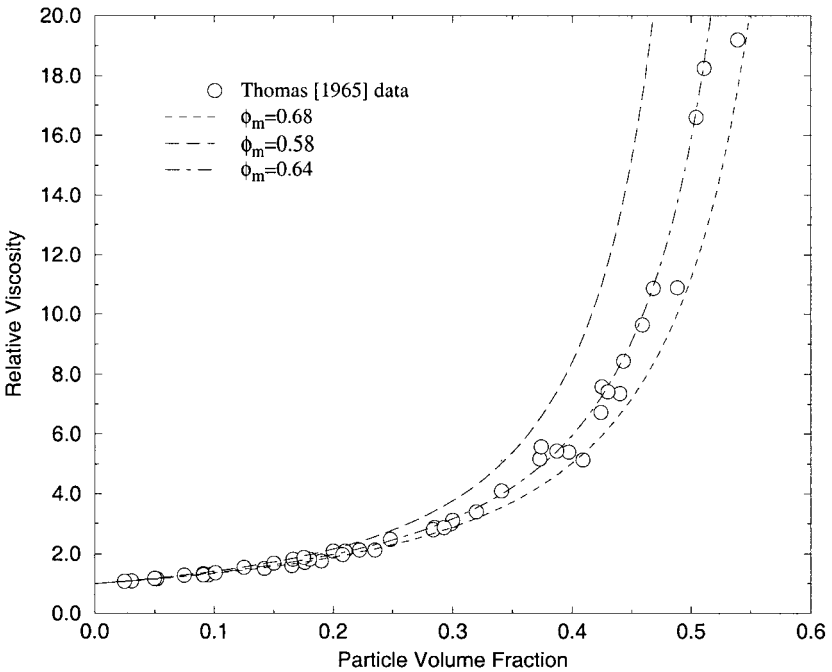

Figure 2. Viscosity data for suspensions of uniform spheres. Lines show Equation (5) with $n = 1.82$ and ϕ_m given in the legend. Phillips *et al.* [4] used $\phi_m = 0.68$.

rearranging Equation (7) and inserting Equation (6) in place of the divergence of velocity gives

$$\frac{\partial \phi}{\partial t} + v \cdot \nabla \phi = - \left(\frac{\rho_f^0 + \phi \Delta \rho}{\rho_s^0 \rho_f^0} \right) \nabla \cdot J_s = - \frac{\rho}{\rho_s^0 \rho_f^0} \nabla \cdot J_s \tag{8}$$

The flux, J_s, can be defined by particle migration from high shear to low shear regions, from high concentration to low concentration, and due to sedimentation or flotation.

$$\frac{J_s}{\rho_s^0} = - \left(\phi D_\phi \nabla (\dot{\gamma} \phi) + \phi^2 \dot{\gamma} D_\mu \nabla (\ln \mu) \right) + f_{\text{hindred}} v_{\text{stokes}} \phi \tag{9}$$

where D_ϕ and D_μ are parameters that must be fit to data, but which scale as the particle radius squared. Note that we are occasionally forced to add small amounts of numerical diffusion to stabilize Equation (9). The first two terms in Equation (9) are the Phillips model [4] and the last term is the extension to settling suspensions proposed by Zhang and Acrivos [19]. According to Phillips [4] a good fit of the data gives the following values of the coefficient:

$$D_\phi = 0.41 a^2 \quad D_\mu = 0.62 a^2 \tag{10}$$

Tetlow *et al.* [29] used experiments and statistical methods to determine a concentration dependent D_ϕ, with a constant D_μ. We follow a similar procedure, but incorporated new NMR data for a range of concentrations [30]. Regression of one-dimensional finite-difference

model against these Couette flow experiments using the same particles but in a neutrally buoyant fluid produced the following diffusion coefficients.

$$D_\phi = 1.05\phi D_\mu \quad D_\mu = 0.651a^2 \tag{11}$$

$\dot{\gamma}$ is the magnitude of the shear-rate tensor and is directly related to the second invariant of the shear-rate tensor [31]. The shear-rate tensor is defined:

$$\underset{\sim}{\dot{\gamma}} = (\nabla v + (\nabla v)^t) \tag{12}$$

and its magnitude is given by:

$$\dot{\gamma} = \sqrt{\tfrac{1}{2}(\underset{\sim}{\dot{\gamma}} : \underset{\sim}{\dot{\gamma}})}. \tag{13}$$

The buoyancy term is written as a Stokes single particle velocity multiplying a factor less than one, termed a hindered settling function. The Stokes velocity is written in terms of the particle radius, a, the density difference between the fluid and solid phases, gravitational acceleration and viscosity of the pure fluid.

$$v_{\text{stokes}} = \frac{2}{9}\frac{a^2(\rho_f^0 - \rho_s^0)\mathbf{g}}{\mu_0} \tag{14}$$

Here we use a hindered settling function similar to Zhang and Acrivos [19] except we use the average concentration or a reference concentration to determine its value together with the local viscosity. This hindered settling function was found to reduce the occurrence of a physical shocks that would occur near the zone of maximum packing and to give realistic looking profiles for the maximum packing zone.

$$f_{\text{hindered}} = \frac{\mu_0(1 - \phi^{\text{average}})}{\mu} \tag{15}$$

The average concentration, ϕ^{average}, is just the initial concentration since the problems that we are solving involve closed flows. We have also experimented with other forms of the hindered settling function including the classical Richardson–Zaki equation [32]:

$$f_{\text{hindered}} = (1 - \phi)^n \tag{16}$$

We found that Richardson–Zaki allows the value of the volume fraction to go above maximum packing. This creates a slope in the concentration in the sediment from maximum packing to one, something that is not seen in experiment. This is because Richardson–Zaki does not go to zero at maximum packing as the Acrivos hindered settling function does. Figure 3 shows the Acrivos hindered settling function plotted with Richardson–Zaki. It is clear from this figure, and from the form of Richardson–Zaki, that it does not go to zero at maximum packing (usually taken to be between 0.58 and 0.68). The Acrivos form of the hindered settling function, on the other hand, will always go to zero at maximum packing since the viscosity diverges at this value of the volume fraction.

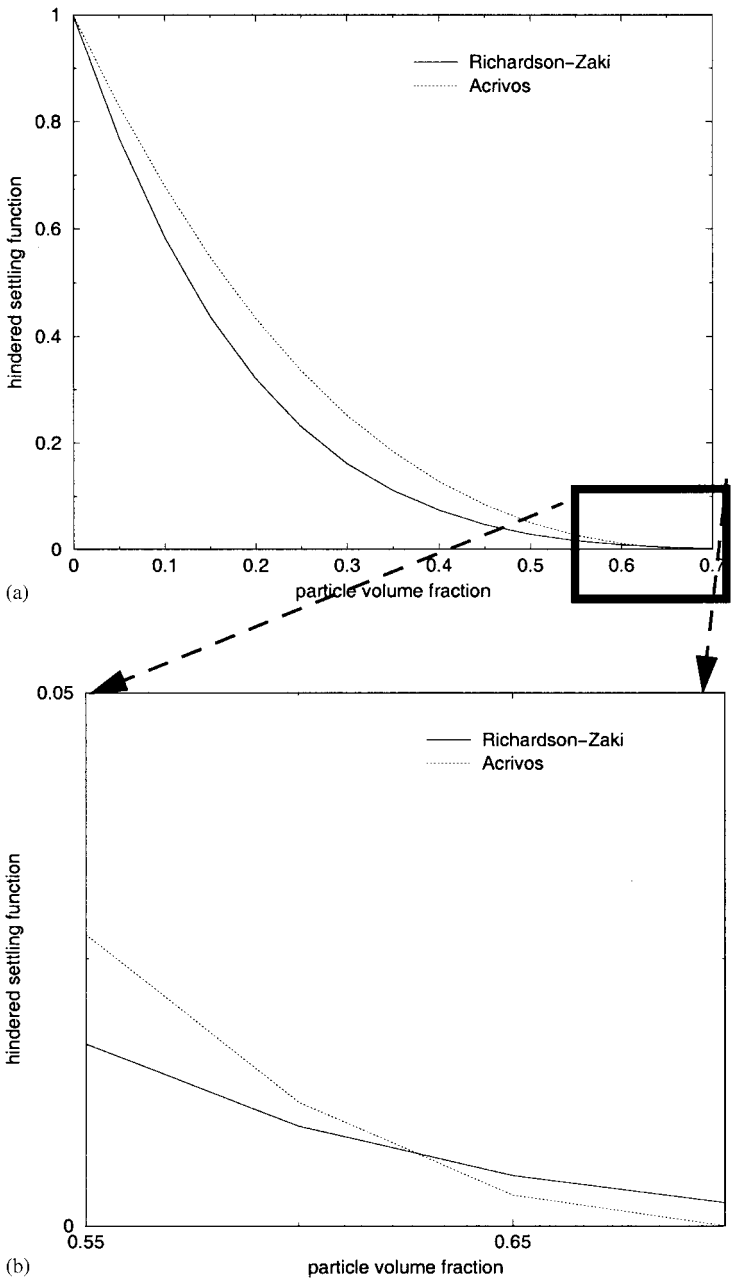

Figure 3. Comparison of different forms of the hindered settling functions. (a) Richardson–Zaki versus Acrivos with region of blow up; (b) blow up of function near maximum packing.

Numerical method

Galerkin finite element method. The equations of interest, the momentum Equation (4), the continuity Equation (6), the species conservation Equation (7), and the scalar magnitude of the shear-rate tensor are discretized with the Galerkin finite element method. The shear-rate must be discretized, since the particle-flux, Equation (8), contains derivatives of this quantity. If we did not have the magnitude of the shear-rate as an unknown, we would introduce second derivatives of the velocity, making the approximation very inaccurate. In the finite element method, second derivatives are generally handled by integrating the diffusion term by parts, moving the part of the differentiation to the weight function. For Equation (8), this cannot be done since the divergence of flux is used in the concentration equation and this term itself is already integrated by parts. Piecewise projection methods can be used to approximate the shear-rate invariant [5], but it has been found that convergence is accelerated by doing a full least squares discretization.

The unknowns of interest are velocity, pressure, particle volume fraction and the shear-rate invariant. For viscous incompressible flow problems, velocity is generally interpolated using a biquadratic shape function, N_i [33].

$$v \approx v_h = \sum_{i=1}^{n} v_i N_i(x, y, z) \tag{17}$$

where v denotes the true velocity solution, v_h denotes the approximate finite element solution and v_i represents the velocities at the nodes. The velocity and the pressure have a constraint between them called the Ladyzhenskaya–Babuska–Brezzi, or LBB, condition that requires the velocity interpolant to be a higher order than the pressure interpolant [34, 35]. If this constraint is not met, the problem becomes over specified and pressure checker-boarding occurs. For this reason, we use a bilinear or linear discontinuous approximation for the pressure.

$$p \approx p_h = \sum_{i=1}^{m} p_i N_i'(x, y, z) \tag{18}$$

No known constraint exists for the particle volume fraction or the shear-rate magnitude so we are free to choose our interpolant. For batch sedimentation we use bilinear approximations for both the volume fraction and the shear-rate, since this is more computationally efficient although it is less accurate. For the Couette studies, we needed the more accurate biquadratic interpolants.

$$\phi \approx \phi_h = \sum_{i=1}^{m} \phi_i N_i''(x, y, z) \tag{19}$$

$$\dot{\gamma} \approx \dot{\gamma}_h = \sum_{i=1}^{m} \dot{\gamma}_i N_i''(x, y, z) \tag{20}$$

The trial functions, Equations (17)–(20), are then substituted into the differential equations in place of the continuous solution to form residual equations. The momentum residual, R_m is:

$$\underset{\sim}{R}_m = \rho \frac{\partial v_h}{\partial t} + \rho v_h \cdot \nabla v_h + \nabla p_h - \nabla \cdot (\mu(\nabla v_h + \nabla v_h^t)) - (\rho_f^0 - \rho_s^0)\phi_h \mathbf{g} \tag{21}$$

The residual equations are then multiplied by weight functions and integrated over the domain. We use the Galerkin finite element method, so the weight functions are chosen to be the shape functions themselves. The finite element solutions are then found so that the weighted residuals become zero in an integrated sense. For the vector momentum equation, we use a vector weighting function. This yields a volume integral over V of the form.

$$\int_V N_i e_\beta \cdot \left(\rho \frac{\partial v_h}{\partial t} + \rho v_h \cdot \nabla v_h + \nabla p_h - \nabla \cdot (\mu(\nabla v_h + \nabla v_h^t)) - (\rho_f^0 - \rho_s^0)\phi_h \mathbf{g} \right) \mathrm{d}V = 0 \tag{22}$$

where e_β is the unit vector in the coordinate directions. The viscous term is integrated by parts to avoid second derivatives of the velocity. This gives

$$\int_V N_i e_\beta \cdot \left(\rho \frac{\partial v_h}{\partial t} + \rho v_h \cdot \nabla v_h + \nabla p_h - (\rho_f^0 - \rho_s^0)\phi_h \mathbf{g} \right) \mathrm{d}V + \int_V \nabla(N_i e_\beta) : \mu(\nabla v_h + \nabla v_h^t)\, \mathrm{d}V - \int_S N_i n \cdot e_\beta \cdot \mu(\nabla v_h + \nabla v_h^t)\, \mathrm{d}S = 0 \tag{23}$$

The integration by parts using the divergence theorem creates surface integrals on S of the domain, where n is the outward facing normal. If no boundary conditions are applied to the momentum equation, the so-called natural boundary condition, the one arising from the integration by parts, will be satisfied in the weak integrated sense [36].

The continuity residual is weighted with the pressure basis function, N_i', and the flux term is integrated by parts.

$$\int_V N_i'(\nabla \cdot v_h)\, \mathrm{d}V + \frac{(\rho_s^0 - \rho_f^0)}{\rho_s^0 \rho_f^0} \int_V \nabla(N_i') \cdot J_s\, \mathrm{d}V - \left(\frac{(\rho_s^0 - \rho_f^0)}{\rho_s^0 \rho_f^0} \right) \int_S N_i' n \cdot J_s\, \mathrm{d}S = 0 \tag{24}$$

This will introduce a natural boundary condition on the continuity equation which says that the flux in the directions normal to the boundary is zero. This is the same natural boundary condition that we get from integrating the diffusion terms in the concentration equation by parts.

The volume fraction residual is weighted with the volume fraction basis function, N_i'', and the flux term is integrated by parts.

$$\int_V N_i'' \left(\frac{\partial \phi}{\partial t} + v_h \cdot \nabla \phi_h \right) \mathrm{d}V + \frac{1}{\rho_s^0 \rho_f^0} \int_V \nabla(\rho N_i'') \cdot J_s\, \mathrm{d}V - \frac{1}{\rho_s^0 \rho_f^0} \int_S N_i'' n \cdot \rho J_s\, \mathrm{d}S = 0 \tag{25}$$

The shear-rate magnitude residual is produced in a similar fashion:

$$\int_V N_i''(\dot{\underset{\sim}{\gamma}}_h - \sqrt{(\nabla v_h + (\nabla v_h)^t) : (\nabla v_h + (\nabla v_h)^t)})\, \mathrm{d}V = 0 \tag{26}$$

Time derivatives are handled with a finite difference discretization. If x represents the solution, the time derivatives would be

$$\frac{\mathrm{d}x}{\mathrm{d}t} = (1 + 2\theta)\left(\frac{x^{k+1} - x^k}{\Delta t^{k+1}}\right) - 2\theta(\dot{x}^k) \tag{27}$$

where θ is a parameter which changes the difference equation from a first order backward Euler scheme ($\theta = 0$) to second order Crank–Nicholson scheme ($\theta = 0.5$) and is set in the input deck, x^{k+1} is the solution at the $k+1$ time step, x^k is the solution at the previous time step, and $\dot{x}^k$ is the time derivative of the solution at the previous time step. For this work, Crank–Nicholson was used. Equation (27) is used for the time derivatives of the velocity in the momentum equation. For the species equation, because of its hyperbolic nature and the steep front that is created during settling, we use a Taylor–Galerkin method for the time integration. For details of the Taylor–Galerkin method see Donea [37].

The weighted residual equations with the difference formula time derivatives substituted in, form a set of nonlinear algebraic equations on each element, which must be solved for the nodal unknowns.

$$F(v_h, p_h, \phi_h, \underset{\sim}{\dot{\gamma}}_h) = 0 \tag{28}$$

We linearize this system with the Newton–Raphson method around the initial guess or previous solution, and rearrange the resulting equation to form an elemental stiffness matrix, K. All the elemental stiffness matrices are assembled to form a global stiffness matrix resulting from contributions from all elements:

$$J(x_n)(x_{n+1} - x_n) = f \tag{29}$$

where the subscript n denotes the iterate for Newton's method. Note that we solve all equations simultaneously in the same matrix in a fully coupled approach [38]. This large matrix equation is then solved by Gaussian elimination to give the new solution. Iterative solvers can also be used to invert Equation (29) if pressure stabilization is used [39]. This is a much more efficient way to solve large two-dimensional and three-dimensional problems. For details of our implementation of pressure stabilization see Cairncross *et al.* [40].

RESULTS

Batch sedimentation

Problem description. The mesh and boundary conditions for the batch settling simulation are given in Figure 4, along with the dimensions of the cylinder in which the particles float. The mesh has 800 elements, 3321 nodes resulting in 9225 unknowns. Our initial goal is to use the diffusive flux model to match simple settling experiments, where there is no imposed flow field. The only motion is created by the movement of the particles themselves. Once sufficient agreement was achieved between settling experiments and simulation, we would move on to more complex flows. The exponent of the Krieger viscosity model (Equation (5)), n, was chosen to be 1.82 for the suspensions, to match available viscosity data. The properties of the material were taken to be those listed in Table I. The simulation we ran will be compared to

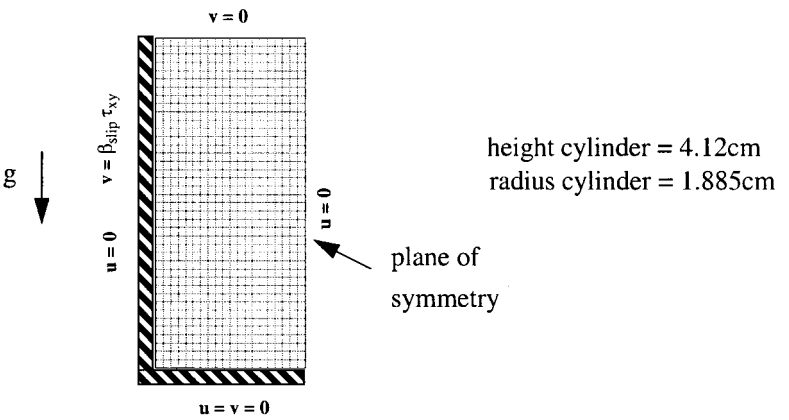

Figure 4. Boundary conditions and mesh for particle settling in a cylinder.

experimental results from NMR visualization of the particle and fluid movement in the results section.

Simulations. The NMR images, when displayed in time sequence as a movie, show definite swirling flow occurring in the bulk of the suspension despite the fact that the suspension is quiescent except for the flotation of particles. The assumption of one-dimensional flow is not necessarily a good one. Although the movement of the clearing layer front is steady and the concentration profile appears to be one-dimensional, the velocity is clearly two-dimensional.

A two-dimensional view of the simulation results is given in Plate 1 for a suspension with $\phi_0 = 0.20$. From this figure, we can see that the concentration profile is truly one dimensional with the particles forming three distinct regions or zones, even though the simulation is two dimensional. Clear fluid is formed at the bottom of the cylinder as the particles float up, since they are lighter than the carrier fluid. A well mixed suspension at the initial volume fraction of 0.20 exists in the middle of the container. At the top of the container, particles pack together to form a zone of maximum packing. Though the concentration field is one dimensional, we can see that the velocity profiles are two dimensional with two sets of buoyancy driven vortices in the suspension and the clear fluid regions. Interestingly enough, these are very similar to the vortices seen in the NMR data, so they may not be numerical artifices. The vortex size also does not change with mesh refinement.

Volume fraction versus height plots are given in Figure 5. This plot contains the NMR data and the simulation results for comparison. The primary NMR data obtained is scaled to represent continuous phase volume fraction as a function of height at 5 min intervals in time. The simulation agrees qualitatively with the data in that we have two fronts that advect towards each other over time: there is a clear fluid front, that is created by particles floating away from the bottom of the cylinder, which moves upward in time and a maximum packing front created by the particles reaching the top of the fluid and packing together as closely as possible. The clear zone front advection matches quite well.

There are, however, discrepancies between the simulation and experiment mostly in the shape of the maximum packing front. In the simulations, we get a very sharp interface, while the data show a much more diffuse interface. It is not clear why this occurs. It is possible

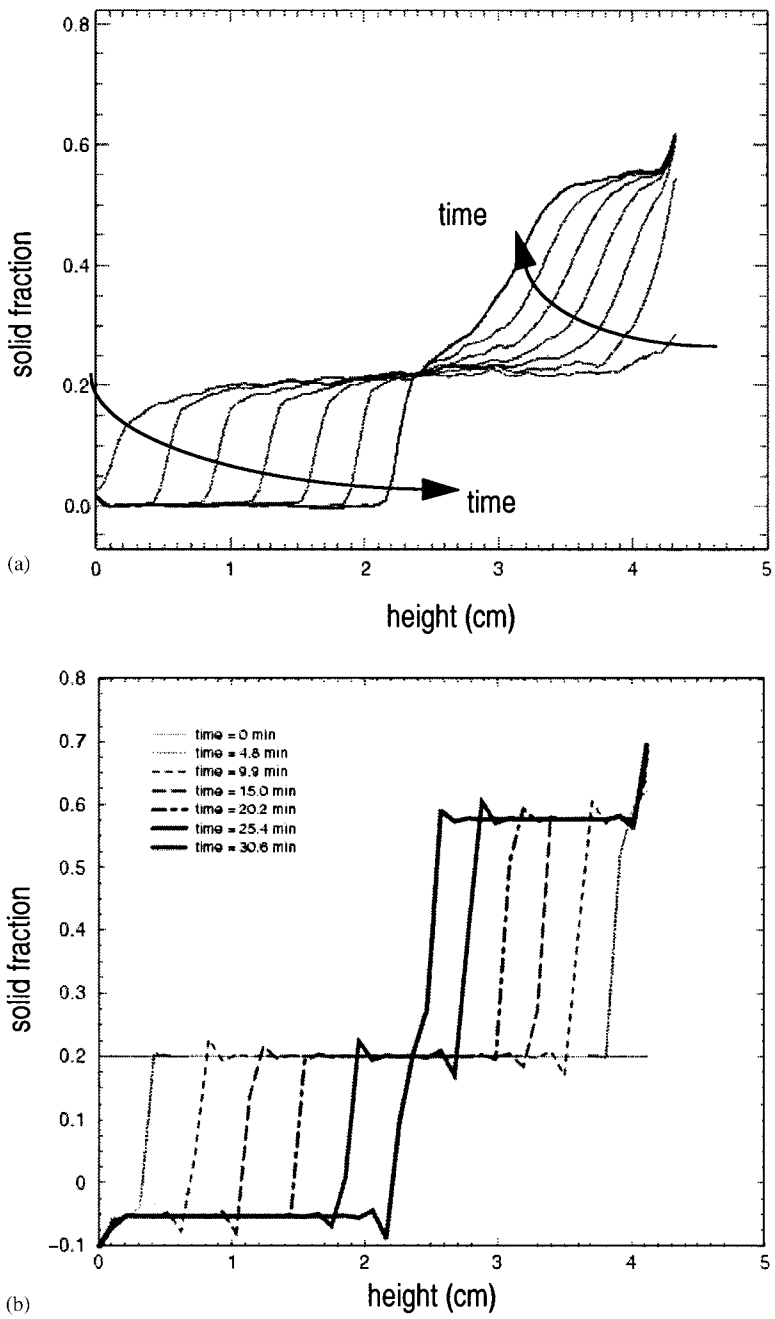

Figure 5. PMMA particle flotation (20 per cent in glycerol solution): particle volume fraction as a function of location in the cylinder. (a) NMR data is given at 5 min intervals; (b) simulation results at approximately 5 min intervals.

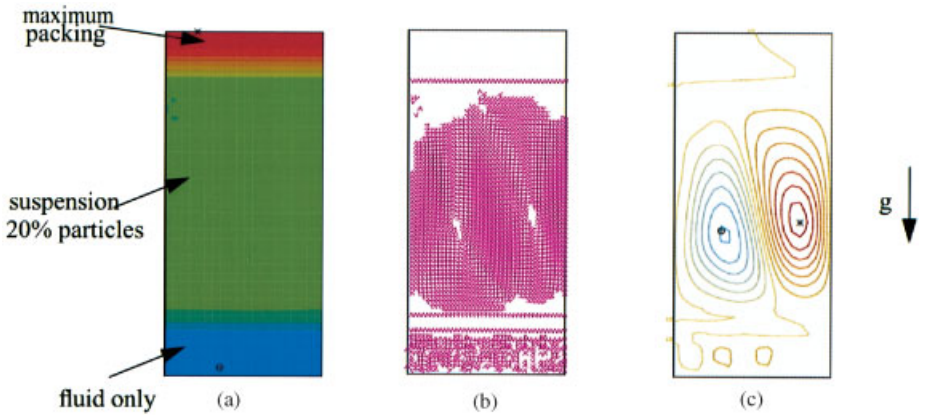

Plate 1. Simulation results for $\phi_0 = 0.20$ at 19.5 min: (a) volume fraction; (b) velocity vectors; (c) streamlines.

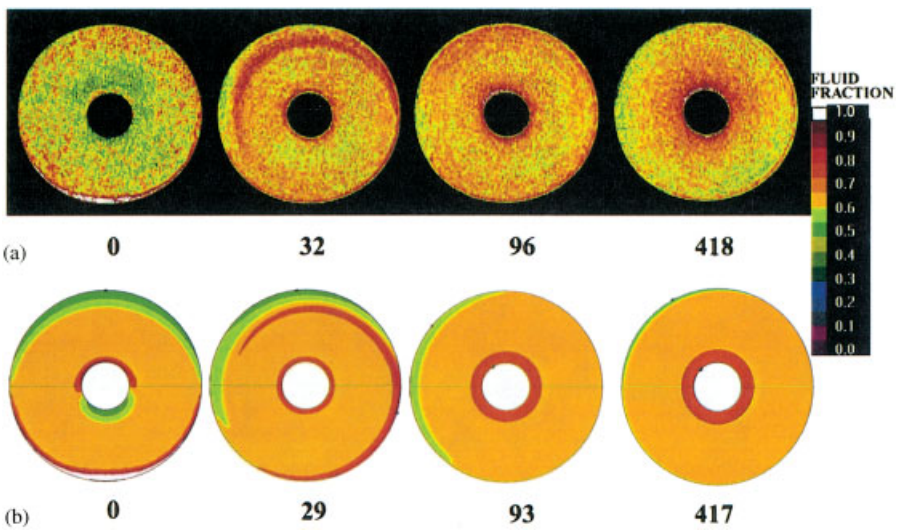

Plate 2. Couette flow concentration profiles as a function of turns of inner rod for initially well-mixed suspension. (a) NMR images; (b) simulation results.

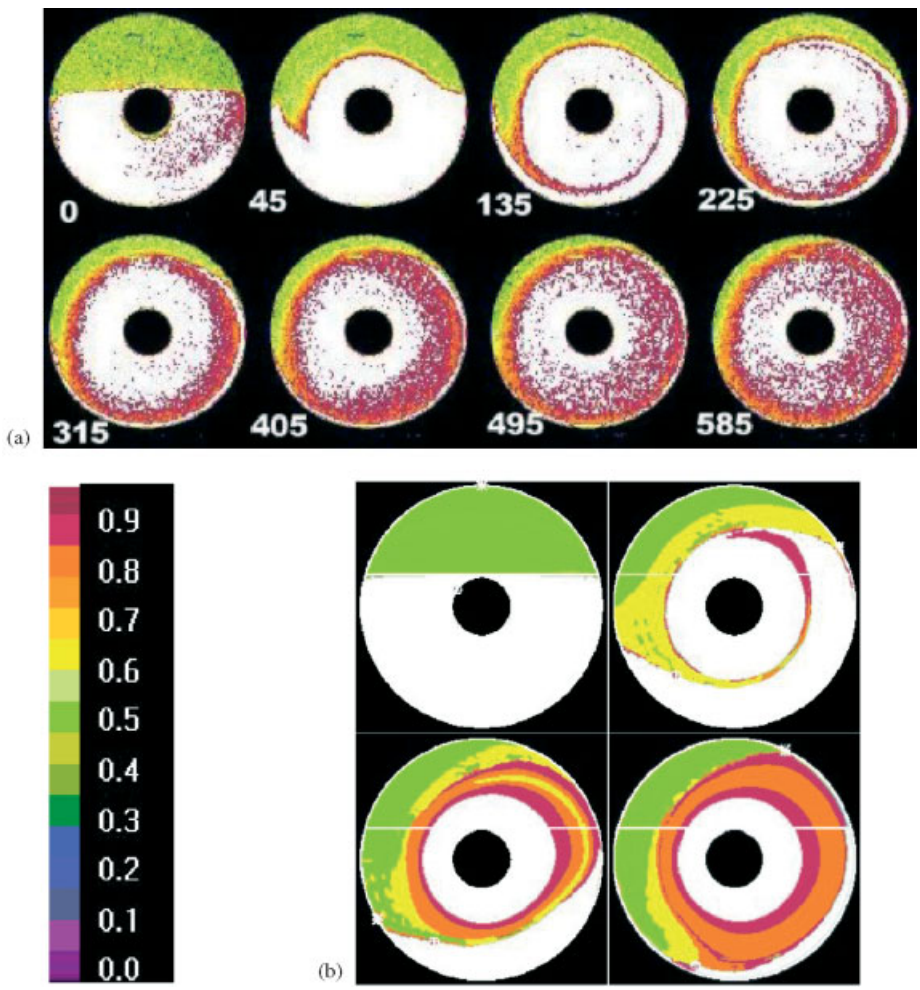

Plate 3. Couette flow concentration profiles at different number of turns. (a) NMR images, 59 per cent top, 0 per cent bottom initially; (b) simulation results.

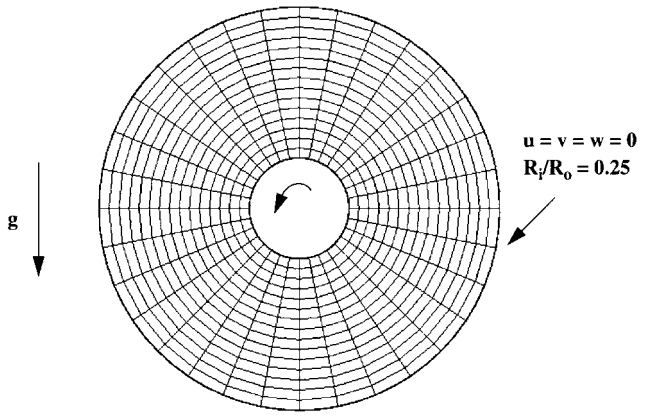

Figure 6. Boundary conditions and mesh for concentric Couette simulations with well mixed initial conditions.

that the large particles feel wall effects that are reflected in the experimental data, but are not represented in the model.

The simulation also has difficulties when the two fronts, or kinematic shocks, come together resulting in wiggles in the solution. The kinematic shocks are created by discontinuities in the density between zones of average concentration, the clear zone, and the maximum packing zone. Oscillations at the clear zone front occurred and also led to negative concentrations at the bottom of the cylinder.

Couette flow: *well mixed initial conditions*

Problem description. Figure 6 shows the boundary conditions and mesh for the wide-gap Couette flow model with the well-mixed initial condition. The same materials, described in Table I, were used except a maximum packing value of 0.64 volume fraction was used. The bulk concentration ϕ_0 of the suspension was set to be 0.35 for this Couette flow study.

Simulation. A comparison of experimental and finite element results for the well-mixed initial condition experiment are presented in Plate 2. Plate 2(a) depicts the NMR images of concentration profiles taken at 0, 32, 96, and 417 turns. Even though the sample loading time has been minimized, the experimental image taken at rest reveals inhomogeneous distribution of particles prior to turning of the inner cylinder. A small, pure fluid zone at the bottom of the device has developed while zones containing as much as 50 per cent volume fraction of particles are scattered near the inner cylinder. Interestingly, the clear zone at the bottom is carried around along the streamlines towards the top of the outer cylinder and persisted even past 100 turns before viscous resuspension remixes the suspended particles in that region. The image taken at 32 turns also reveal a small packed zone to the left of the low concentration band. This is probably due to accumulation of particles displaced by the low concentration band. The concentration profile at 417 turns no longer shows signs of the initial inhomogeneity, instead it shows pronounced radial gradient particle concentration due to shear-induced migration.

Snapshots of simulated particle concentration at similar time points are shown in Plate 2(b). Based on what was observed experimentally, the assumption of initially 'uniform' solution is not applied to this problem. Instead, the simulation allowed the particles to float quiescently until a clear zone with the size comparable to that observed in the experiment has developed; this consisted of about 5 min flotation without turning of the inner cylinder in both the experiment and simulation. Interestingly, when the simulations were carried out without matching the initial conditions the results matched the experiments qualitatively, but did not capture the transient correct behavior.

In the first snapshot, the model-generated profile shows different regions of low and high particle concentrations. Particles have packed near the bottom of the inner cylinder as well as along the top wall of the outer cylinder. Other than the clear zone created at the bottom, there is also a small band of low concentration particles at the top of the inner cylinder. After 29 turns, the regions of high and low concentrations along the outer cylinder still remain, while the inhomogeneity along the inner cylinder remixes quickly as shear-induced migration becomes dominant in that region. Although the packed zone at the top of the device is not observed in the experiment, the comparison of the dynamic profiles show good qualitative agreement between the model and the experiment. At 93 turns, the high concentration band along the outer cylinder thins out as more particles remix into the bulk. Eventually the band disappears around 160 turns, well before the formation of another high concentration region at the top of the outer cylinder, clearly visible in that last snapshot at 418 turns. Such a concentrated region is not evident in the experiment, but can be viewed as a region where the suspended particles are held in place as its flotation rate cancels out the convective/diffusive flux.

Couette flow: sedimented initial condition

Problem description. The same materials and parameters were used as in the well-mixed Couette problem. For the second study, although the overall particle concentration was 0.2, it was divided between a particle-rich and particle-free region, as shown in Figure 7. The initial

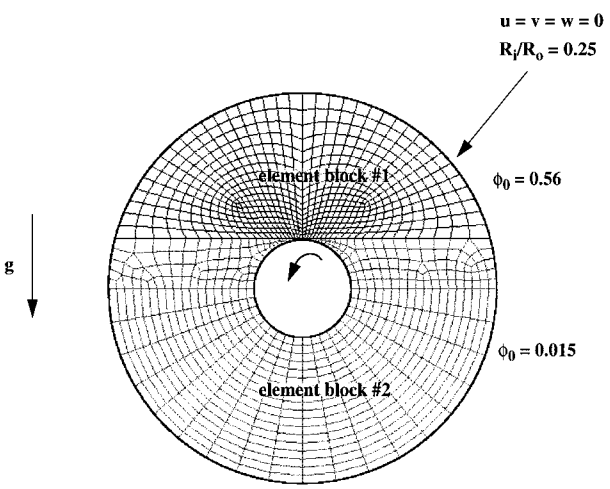

Figure 7. Boundary conditions and mesh for concentric Couette with sedimented initial conditions.

attempt to simulate this case using the mesh for the previous example was unsuccessful since refinement of mesh at the particle-rich and particle-free interface could not be accomplished as it evolved with time. Instead, a different, finer mesh was used for this simulation. The initial concentration of two distinct element blocks are set as close to the experimental values as possible to yield a total of 0.2.

Simulation. Plate 3 shows a comparison of the NMR and finite element results for the initially sedimented suspension. In Plate 3(a), the NMR images for the second experiment indicate that the particles have packed to the top of the Couette gap before the motor is turned on. The concentration of the packed zone is 59 per cent, or 1 per cent over its theoretical maximum packing value. This is conceivable since particles of one size may exhibit some degree of polydispersity. Contrary to the first experiment, though, this packed zone thins out at a slower rate. This may be attributed to the inertial effect as it dominates the dynamics initially. Any mixing at higher turns occurs close to the outer cylinder wall while the region around the inner cylinder wall remains devoid of particles due to shear-induced migration.

The simulated concentration profiles in Plate 3(b) agree qualitatively with the NMR imaging results. An initial two-phase mixture moves in almost solid body rotation of the maximum packing zone. In fact, simulations that were run without particle diffusion show almost identical early-time results. However, the early mixing in the simulation occurs more quickly than in the experiment. By 226 turns the effects of shear-induced migration can be seen. This migration retards the mixing of the outer layers and the simulation actually begins to lag the experimental results. By 586 turns, the maximum packing layer near the outer left side of the cylinder is larger in the simulation than in the experiment. However, qualitative features, such as the asymmetry created by buoyancy effects interacting with the turn direction, are preserved.

There are a number of reasons that may have caused the discrepancies. To simulate solid-like behavior of the maximum packing zone, we set the viscosity to ramp to a very large value (to approximate infinity) as the concentration reaches maximum packing. However, the material in this zone cannot support stresses as a true solid would. Also, the resuspension mechanism, where individual particles peal off the packed zone, cannot be mimicked by a continuum equation. Potentially at two-phase model could be more successful at capturing the resuspension behavior. More accurate dynamics may also be achieved with a finer mesh and a better numerical scheme that can handle time-variant concentration discontinuities. The numerical method used has trouble capturing behavior when concentrations vary from maximum packing to pure fluid over an element. The kinematic shock and discontinuous concentration lead to numerical instabilities and oscillations in the solution.

CONCLUSIONS

We have achieved good qualitative agreement between the simulations and the experiments. However, discrepancies exist between the shape of the concentration profiles for the quiescent sedimentation data and the numerical model. Numerical difficulties also occur in situations where large changes in concentration and thus viscosity occur over short distances. For this reason, the model of the shear flow in the well-mixed wide-gap Couette was better behaved than the quiescent settling and the Couette with the sedimented initial condition. Many improvements to the model are being investigated to improve the agreement between

the numerical results and the experimental data. Following Beckermann *et al.* [41] we plan on implementing the solid–liquid phase change with a porous Brinkman source term that will slow the flow depending on the particle volume fraction. This is known to be a more robust approach to phase-change than solely ramping the viscosity.

ACKNOWLEDGEMENTS

This work was supported by the United States Department of Energy under Contract DE-AC04-94AL85000. Sandia is a multiprogram laboratory operated by Sandia Corporation, a Lockheed Martin Company, for the United States Department of Energy. The authors would like to acknowledge support for this work by the U.S. Department of Energy, Office of Basic Energy Sciences and Mathematical, Information and Computational Science Division for a 'Grand Challenge' grant. Partial funding for the work done at the Naval Air Warfare Center was also provided by SDIO/IST and managed by the Office of Naval Research.

REFERENCES

1. Karnis A, Goldsmith HL, Mason SG. The kinetics of flowing dispersions I. Concentrated suspensions of rigid particles. *Journal of Colloid Interface Science* 1966; **22**:531–533.
2. Leighton D, Acrivos A. The shear-induced migration of particles in concentrated suspensions. *Journal of Fluid Mechanics* 1987; **181**:415–439.
3. Abbott JR, Tetlow N, Graham AL, Altobelli SA, Fukushima E, Mondy LA, Stephens TS. Experimental observations of particle migration in concentrated suspensions: Couette flow. *Journal of Rheology* 1991; **35**: 773–795.
4. Phillips RJ, Armstrong RC, Brown RA, Graham AL, Abott JR. A constitutive equation for concentrated suspensions that accounts for shear-induced particle migration. *Physics of Fluids A* 1992; **4**:30–40.
5. Subia SR, Ingber MS, Mondy LA, Altobelli SA, Graham AL. Modelling of concentrated suspensions using a continuum constitutive equation. *Journal of Fluid Mechanics* 1998; **373**:193–219.
6. Leighton D, Acrivos A. Viscous resuspension. *Chemical Engineering Science* 1986; **6**:1377–1384.
7. Chapman BK, Leighton DT, Jr. Dynamics viscous resuspension. *International Journal of Multiphase Flow* 1991; **17**:469–483.
8. Acrivos A, Mauri R, Fan X. Shear-induced resuspension in a Couette device. *International Journal of Multiphase Flow* 1993; **19**:797–802.
9. Krishnan GP, Leighton DT. Dynamic viscous resuspension of bidisperse suspensions—I. Effective diffusivity. *International Journal of Multiphase Flow* 1995; **21**:721.
10. Hallworth MA, Huppert HE. Abrupt transitions in high-concentration, particle-driven gravity currents. *Physics of Fluids* 1998; **10**:1083.
11. Breedveld V, Van Den Ende D, Tripathi A, Acrivos A. The measurement of the shear-induced particle and fluid tracer diffusivities in concentrated suspensions by a novel method. *Journal of Fluid Mechanics* 1998; **375**:297–318.
12. Andrews MJ, O'Rourke PJ. The multiphase particle-in-cell (MP-PIC) method for dense particulate flows. *International Journal of Multiphase Flow* 1996; **22**:379–402.
13. Hu HH. Direct simulation of flows of solid–liquid mixtures. *International Journal of Multiphase Flow* 1996; **22**:335.
14. Morris JF, Brady JF. Pressure-driven flow of a suspension: buoyancy effects. *International Journal of Multiphase Flow* 1998; **24**:105–130.
15. Schaflinger U, Acrivos A, Zhang K. Viscous resuspension of a sediment within a laminar and stratified flow. *International Journal of Multiphase Flow* 1990; **16**:567–578.
16. Shauly A, Wachs A, Nir A. Shear-induced particle resuspension in settling polydisperse concentrated suspension. *International Journal of Multiphase Flow* 2000; **26**:1–15.
17. Miskin I, Elliot E, Ingham DB, Hammond PS. Steady suspension flows into two-dimensional horizontal and inclined channels. *International Journal of Multiphase Flow* 1996; **22**:1223.
18. Miskin I, Elliot E, Ingham DB, Hammond PS. The viscous resuspension of particles in an inclined rectangular fracture. *International Journal of Multiphase Flow* 1996; **22**:403.
19. Zhang K, Acrivos A. Viscous resuspension in fully developed laminar pipe flows. *International Journal of Multiphase Flow* 1994; **20**:579–591.
20. Probstein RF. *Physiochemical Hydrodynamics: an Introduction*. Butterworths: Boston, 1989.

21. Kynch GJ. A theory of sedimentation. *Transactions on Faraday Society* 1952; **48**:166–176.
22. Brodkey RS. *The Phenomena of Fluid Motions*. Addison-Wesley: Reading, MA, 1967.
23. Turney MA, Cheung MK, McCarthy MJ, Powell RL. Magnetic resonance imaging study of sedimenting suspensions of noncolloidal spheres. *Physics of Fluids* 1995; **7**:904–911.
24. Lee S, Jang Y, Choi C, Lee T. Combined effect of sedimentation velocity fluctuation and self-sharpening of interface broadening. *Physics of Fluids A* 1992; **4**:2601–2606.
25. Callaghan PT. *Principles of Nuclear Magnetic Resonance Microscopy*. Oxford University Press: New York, 1991.
26. Krieger IM. Rheology of monodisperse lattices. *Advances in Colloidal Interface Science* 1972; **3**:111–136.
27. Thomas DG. Transport characteristics of suspensions VIII: a note on the viscosity of Newtonian suspensions of uniform spherical particles. *Journal of Colloid Science* 1965; **20**:267–277.
28. Mondy LA, Pacheco G, Henfling J, Ingber MS, Graham AL, Brenner H. Spinning ball rheometry in concentrated suspension. *Journal of Fluid Mechanics* 2002; submitted.
29. Tetlow N, Graham AL, Ingber MS, Subia SR, Mondy LA, Altobelli SA. Particle migration in a Couette apparatus: Experimental and modeling. *Journal of Rheology* 1998; **42**:307–327.
30. Abbott JR. Personal Communication 2000.
31. Bird RB, Armstrong RC, Hassager O. *Dynamics of Polymeric Liquids*. Wiley: New York, 1987.
32. Bird RB, Stewart WE, Lightfoot EN. *Transport Phenomena*. Wiley: New York, 1960.
33. Fortin M, Fortin A. Experiments with several elements for viscous incompressible flows. *International Journal for Numerical Methods in Fluids* 1985; **10**:911–928.
34. Reddy JN, Gartling DK. *The Finite Element Method in Heat Transfer and Fluid Dynamics, 2nd Edition*. CRC Press: Boca Raton, 2001.
35. Oden JT, Carey GF. *Finite Elements*, *Mathematical Aspects*, *Volume IV*. Prentice-Hall: Englewood Cliffs, New Jersey, 1983.
36. Finlayson BA. Orthogonal collocation on finite elements-progress and potential. *Mathematics and Computers in Simulation* 1980; **22**:11–17.
37. Donea J. A Taylor-Galerkin method for convective transport problems. *International Journal for Numerical Methods in Engineering* 1984; **20**:101–119.
38. Schunk PR, Sackinger PA, Rao RR, Chen KS, Cairncross RA, Baer TA, Labreche DA. GOMA 2.0. Sandia National Laboratories, SAND97-2404, 1997.
39. Hughes TRJ, Franca LP, Balestra M. A new finite element formulation for computational fluid dynamics: V. Circumventing the Babuska–Brezzi condition: a stable Petrov–Galerkin formulation of the Stokes problem accommodating equal order interpolation. *Computational Methods in Applied Mechanics and Engineering* 1986; **59**:85.
40. Cairncross RA, Schunk PR, Baer TA, Rao RR, Sackinger PA. A finite element method for free surface flow of incompressible fluids in three dimensions. Part I. Boundary fitted mesh motion. *International Journal for Numerical Methods in Fluids* 2000; **33**:373–403.
41. Beckermann C, Diepers HJ, Steinbach I, Karma A, Tong X. Modeling melt convection in phase-field simulations of solidification. *Journal of Computational Physics* 1999; **154**:468–496.

